CHEMISTRY & SUSTAINABILITY

CHEMSUSCHEM

ENERGY & MATERIALS

Accepted Article

Title: Controlled Deposition and Performance Optimization of Perovskite Solar Cells Using Ultrasonic Spray-Coating Photoactive Layers

Authors: Wei-Chieh Chang, Ding-Hung Lan, Kun-Mu Lee, Xiao-Feng Wang, and Cheng-Liang Liu

To be cited as: *ChemSusChem* 10.1002/cssc.201601711

Link to VoR: http://dx.doi.org/10.1002/cssc.201601711

A Journal of

ChemPubSoc Europe

WILEY-VCH

www.chemsuschem.org

WILEY-VCH

FULL PAPER

Controlled Deposition and Performance Optimization of Perovskite Solar Cells Using Ultrasonic Spray-Coating Photoactive Layers

Wei-Chieh Chang,[a] Ding-Hung Lan,[a] Kun-Mu Lee,[a,b] Xiao-Feng Wang,[c] and Cheng-Liang Liu*[a]

Abstract: This study investigates novel film deposition technique, ultrasonic spray-coating, for use in photoactive layer of perovskite solar cell. Stable atomization and facile fabrication of perovskite thin films by ultrasonic spray-coating are achieved in an one-step method via manipulating the ink formulation such as solution concentration, precursor composition and mixing solvent ratio, and the drying kinetic such as post-annealing temperature. The performance of perovskite solar cells is mainly influenced by the intrinsic film morphology and crystalline orientation of the deposited perovskite layer. By proper optimizing the spreading and drying condition of ink, we achieve ultrasonic spray-coated perovskite photovoltaic devices with maximum power efficiency (*PCE*) of 11.30%, with fill factor (*FF*), short circuit current (J_{sc}) and open circuit voltage (V_{oc}) of 73.6%, 19.7 mA cm^{-1} and 0.78 V, respectively. Notably, the average *PCE* reaches above 10% attributed to the large-sized flower-like perovskite crystal with orientation along (112)/(200) and (224)/(440) direction. Thus, the ultrasonic spray-coating method for perovskite photoactive layers with combined advantages of good photovoltaic performance results and benefit from cost and processing have the capability of scaling into large scale commercial production.

Introduction

Organic-inorganic metal halide perovskite solar cells are one of the most attractive and efficient emerging thin film photovoltaics, with the reported power conversion efficiency (*PCE*) of rising from 3.8% to over 20% during the span of only few years.[1-4] Perovskite light absorber was first attempted to include in the dye-sensitized solar cell structure by Miyasaka et al in 2009.[1] However, this work was little paid attention due to dissolution problem of perovskite in polar liquid electrolyte. Later on, perovskite photovoltaics was triggered by the report on long-term stable and higher efficiency solid-state perovskite solar cell.[2] There is a wide range of processing techniques ranging from solution to vacuum evaporation which can be used for fabrication of highly efficient devices with either mesoscopic or planar cell architecture. Particularly, solution-processed perovskite light harvesting layer is our interest due to low-cost, scalable and vacuum-free construction method.[5, 6] Up to now, it is still challenging in the fabrication of high quality perovskite film with controlled morphology, high surface coverage and large grain domain for high performance solution-processed perovskite solar cell. A variety of effective approaches to manipulate the growth of perovskite crystals in solution-processed system especially in the planer heterojunction in order to achieve the optimized morphology are densely investigated.[7-9] A desired perovskite film deposition and crystalline formation can be found by adopting proper deposition methods (one/two or multi-steps)[10-14] and tuning precursors-related parameters (solution concentration,[15, 16] precursor ratio[17-20] and professional solvent engineering[21-24]), solution-coating variables[25-29] (processing/post-processing temperature/time, etc), and interfacial engineering[30-32], etc.

Together with enhanced photovoltaic device performance, it is important to improve the solution processability that accelerates to utilize perovskite materials. Currently, perovskite films are mainly made via laboratory-level deposition methods, e.g., spin-coating and dip-coating.[5, 6] To succeed as a useful manufacturing skill, a specific deposition approach must be scalable while still producing the films with high quality.[20] Spray-coating is one of the mature thin film fabrication techniques in industrial coatings which can be potentially scalable to large areas and may be also applied for perovskite devices with tailed photovoltaic performance. Spray-coating technique includes the several steps of atomization of solution, droplet flight onto the target, droplet spreading, crystallization and film formation with the help of carrier gas. In 2014, Lidzey's group first reported the use of spray deposition for efficient planar heterojunction mixed-halide perovskite solar cells.[33] After that, several numbers of recent reports further extended new opportunities for spray technology in the field of perovskite solar cell.[34-48] The goal to achieve a printable perovskite solar cells using spray-coating can be justified by the processability of depositing solutions and post-processing treatment in a simple and low-cost way. Given that spray deposition has great potential in continuous process, fundamental investigation on how aforementioned key factors affect the

[a] W.-C Chang, D.-H. Lan, Prof. K.-M. Lee, Prof. C.-L. Liu
Department of Chemical and Materials Engineering
National Central University
Taoyuan, 32001 Taiwan
E-mail: clliu@ncu.edu.tw
[b] Prof. K.-M. Lee
Research Center for New Generation Photovoltaics
National Central University
Taoyuan, 32001 Taiwan
[c Prof. X.-F. Wang
Key Laboratory of Physics and Technology for Advanced Batteries,
Ministry of Education
College of Physics
Jilin University
Changchun, 130012 China

Supporting information for this article is given via a link at the end of the document.

equality and the performance of solution-processed perovskite thin film used in solar cells has to be more addressed.

One of commonly used types of spray-coating is based on ultrasonic where atomization is caused by ultrasonic frequencies. Ultrasonic vibration helps to mix the precursor homogeneously and improve the film uniformity. Herein, the surface properties of ultrasonic spray-coated $CH_3NH_3PbI_3$ thin film layer can be investigated by varied precursor and heating conditions, which can be correlated of the photovoltaic performance. The thickness, surface morphologies, grain size and crystal orientation of resulting perovskite films can be altered not only by concentration of stoichiometric solution of PbI_2 and CH_3NH_3I in different ratios of dimethylsulfoxide (DMSO) and γ-butyrolactone (GBL) solvent mixture but also by post-annealing temperature under the one-step coating process. After fully optimizing the processing parameters, large crystalline domain of perovskite layer surface with a flower-like pattern radiating from the center lead to a *PCE* of 11.30% in maximum and 10.37±0.91% in average, respectively. Thus, it provides insights for future work to further optimize the device performance as well as supply scalable techniques for large deposition of perovskite film via ultrasonic spray-coating.

Results and Discussion

The ultrasonic spray deposition of perovskite layer for planar photovoltaic application was demonstrated here by rationally improving the device performance through precursor total concentration/composition, mixing solvents volume ratio and annealing temperature. The schematic of the computer numeric controlled spray system equipped with a servo-motorized nozzle head was shown in Figure S1 of SI. First, the perovskite films were fabricated by one-step method and their thicknesses were controlled by changing the concentrations (9~21 wt%) of precursor (1:1 of PbI_2:CH_3NH_3I in DMSO:GBL (5:5 in vol)) with a fixed spraying procedure followed by annealing at 100 °C for 30 min. The thicknesses of the perovskite films increase with the increase of the concentration, ranging between 200 and 600 nm (Figure S2 of SI). The optical absorption spectra of perovskite films with different thicknesses were measured, as shown in Figure S3(a) of SI. The absorption onset of $CH_3NH_3PbI_3$ film was observed at a ~785 nm wavelength (1.58 eV) with a broad band from near-infrared to visible region. Besides, the absorbance intensity enhances obviously with higher precursor concentration, mainly due to more absorbed light from thicker perovskite film. To verify the precursor concentration on film formation, planar heterojunction perovskite solar cells employing the configuration of ITO/PEDOT:PSS/$CH_3NH_3PbI_3$/C_{60}/BCP/Al were fabricated. Figure 1 presents the *J-V* curves obtained from the studied devices with using different perovskite thicknesses (prepared from different precursor solution concentrations), and the corresponding photovoltaic parameters are summarized in Table 1. The device fabricated with a thickness of ~200 nm/a total precursor concentration of 9 wt% exhibits a lower average *PCE* of 4.07±1.28% In contrast, the device with suitable perovskite thickness of ~450 nm and concentration of 15 wt% presents the best performance with *PCE* of 11.30%, a short circuit current (J_{sc}) of 19.7 mA cm^{-2}, an open circuit voltage (V_{oc}) of 0.78 V and a fill factor (*FF*) of 73.6% based on champion cell. The XRD peaks observed at 19.8° and 40.5° represent strong (112)/(200) and (224)/(400) crystal planes of $CH_3NH_3PbI_3$, respectively, which agrees with previous results on XRD patterns (Figure S3(b) of SI).[22] Weak peak at 12.5° indicates slight PbI_2 impurities inside the perovskite film. Besides, XRD peak intensity increases as the perovskite thickness increases, suggesting the strong dependence of film crystallinity on the concentration of precursor solution. All the microscopic perovskite films with different thicknesses as observed by SEM illustrate similar flower-like growth crystal structures,[12, 20-22] except for their grain sizes (Figure S4 of SI). Obviously, the smaller grain (50 μm in size) of the perovskite crystal fabricated from 9 wt% of precursor concentration may enable the overall bulk defect density originated from the gap region. In this case, the lowest *PCE* of the thinner perovskite film as evidenced by structural and optical properties is mainly attributed to low light absorption, the insufficient charge transport across the incomplete surface and low crystallinity. Therefore, the larger grain size with optimized

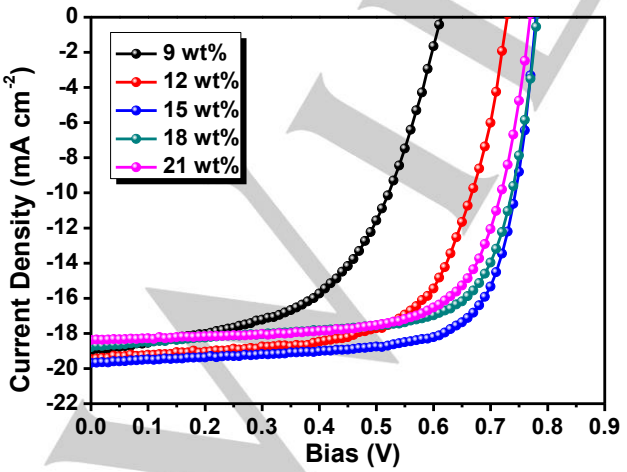

Figure 1. *J-V* curves of ultrasonic spray-coated $CH_3NH_3PbI_3$ solar cells with different precursor concentrations of 9%, 12%, 15%, 18%, and 21%, respectively.

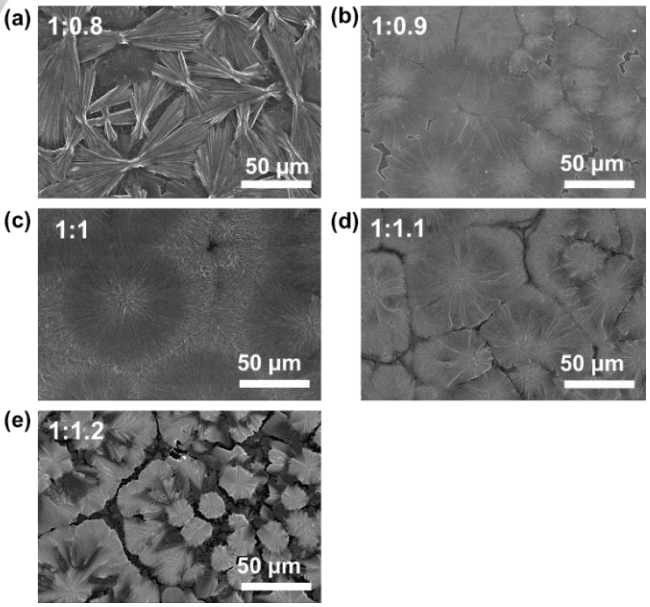

Figure 2. SEM images of ultrasonic spray-coated $CH_3NH_3PbI_3$ thin films made from (a) 1:0.8, (b) 1:0.9, (c) 1:1, (d) 1:1.1, and (e) 1:1.2 PbI_2:CH_3NH_3I molar ratio solution.

Table 1. Photovoltaic parameters of planar heterojunction perovskite solar cell using ultrasonic spray deposition method with different processing parameters.

Concn. (wt%)	PbI_2: CH_3NH_3I (mol:mol)	DMSO:GBL (vol:vol)	T_{anneal} (°C)	*Jsc* (mA cm^{-2})	V_{oc} (V)	*FF* (%)	*PCE* (%)
9	1:1	5:5	110	18.4±1.0 (19.0)	0.45±0.10 (0.61)	50.6±3.6 (54.9)	4.07±1.28 (6.40)
12	1:1	5:5	110	19.9±0.9 (19.5)	0.65±0.08 (0.73)	61.5±4.5 (66.1)	7.64±1.46 (9.38)
15	1:0.8	5:5	110	9.5±1.7 (10.9)	0.70±0.06 (0.75)	57.1±7.6 (68.6)	3.78±0.93 (5.62)
15	1:0.9	5:5	110	15.1±2.1 (16.7)	0.71±0.06 (0.78)	62.3±4.9 (67.2)	6.77±1.85 (8.79)
15	1:1	10:0	110	15.0±1.3 (15.6)	0.76±0.02 (0.77)	62.0±4.6 (64.8)	7.01±0.74 (7.72)
15	1:1	7:3	110	17.2±1.0 (16.6)	0.67±0.04 (0.73)	62.3±4.9 (64.3)	7.37±1.19 (7.82)
15	1:1	5:5	90	16.2±2.4 (18.0)	0.25±0.05 (0.25)	40.5±6.2 (46.6)	1.62±0.53 (2.07)
15	1:1	5:5	100	18.3±0.7 (17.9)	0.58±0.05 (0.65)	56.1±4.5 (61.0)	5.95±1.05 (7.11)
15	1:1	5:5	110	19.3±0.7 (19.7)	0.76±0.03 (0.78)	70.9±2.8 (73.6)	10.37±0.91 (11.30)
15	1:1	5:5	120	18.3±1.2 (18.6)	0.76±0.03 (0.79)	62.0±6.4 (70.4)	8.69±1.43 (10.31)
15	1:1	5:5	130	15.6±1.1 (17.2)	0.70±0.07 (0.76)	53.6±6.6 (62.6)	6.37±1.39 (8.15)
15	1:1	3:7	110	17.4±3.1 (19.3)	0.67±0.07 (0.70)	60.6±4.7 (63.5)	7.00±1.03 (8.57)
15	1:1	0:10	110	16.9±1.0 (17.5)	0.47±0.10 (0.62)	51.6±10.9 (49.8)	4.17±1.50 (5.82)
15	1:1.1	5:5	110	20.7±0.4 (21.1)	0.76±0.05 (0.78)	55.7±7.6 (63.7)	8.79±1.55 (10.52)
15	1:1.2	5:5	110	2.61±1.5 (4.12)	0.04±0.03 (0.08)	19.3±10.6 (25.2)	0.04±0.03 (0.08)
18	1:1	5:5	110	18.4±0.4 (18.8)	0.76±0.02 (0.78)	70.8±1.8 (71.6)	9.94±0.37 (10.51)
21	1:1	5:5	110	16.9±1.9 (18.4)	0.76±0.01 (0.77)	70.0±3.1 (70.8)	8.95±1.13 (10.00)

thickness (~450 nm) of the perovskite thin film fabricated from 15 wt% of precursor concentration reduces the charge recombination at the grain boundaries and significantly improves the *FF* and V_{oc}.[12, 28] In the following optimized procedures, the total precursor concentration is fixed at 15 wt% for further device testing.

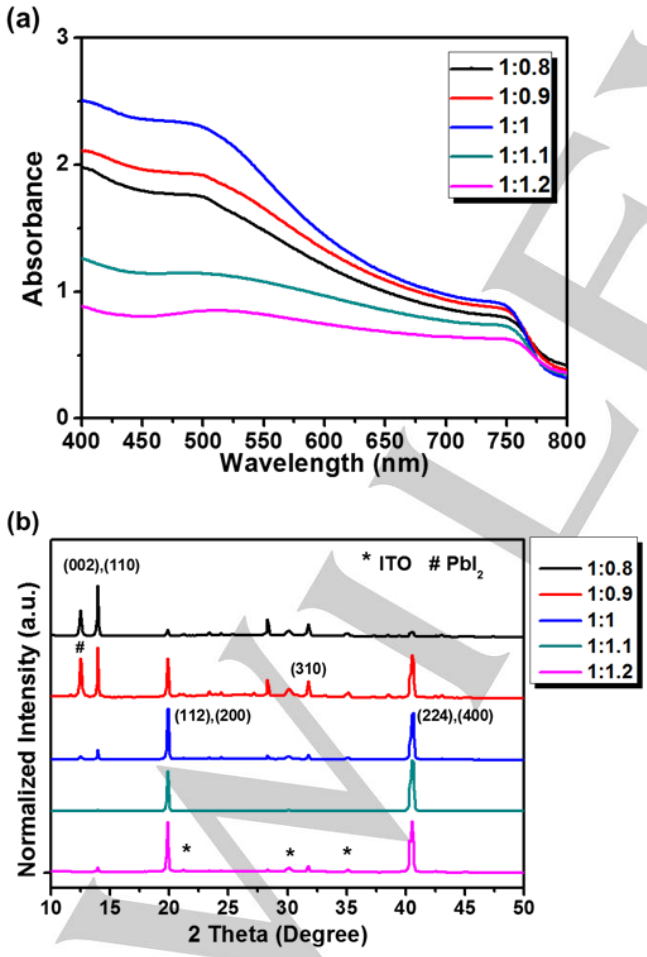

Figure 3. (a) Absorption spectrum and (b) XRD patterns of ultrasonic spray-coated $CH_3NH_3PbI_3$ thin films made from 1:0.8, 1:0.9, 1:1, 1:1.1, and 1:1.2 PbI_2:CH_3NH_3I molar ratio solution.

The formulation of the precursor inks is closely correlated with the $CH_3NH_3PbI_3$ perovskite film quality as well as the *PCE* of photovoltaic device. Next, the perovskite thin films were deposited by ultrasonic spray-coating the precursor composed of PbI_2 and CH_3NH_3I with desired molar ratios varied from 1:0.8 to 1:1.2. The SEM images shown in Figure 2 reveal the film morphology evolution from needle-like to mixed needle-/flower-like and flower-like for precursor molar ratio of 1:0.8, 1:0.9 and 1:1, respectively. With the further change in PbI_2:CH_3NH_3I molar ratio less than 1:1, the flower-like morphologies with circular-shaped domain still remains. However, the average grain size reduces continuously and rougher surface can be distinguished as the precursor molar ratio decreases up to 1:1.2. The perovskite film with optimized 1:1 precursor ratio clearly decreases the gap between the grains, and it can also be found that the enhanced uniformity of perovskite film with considerably reduced scattering contributes to significant stronger optical absorption (Figure 3(a)) which is beneficial for enhanced photon harvesting capability. For XRD analysis (Figure 3(b)), two specific points between the differences on the XRD patterns should be noted here. For the precursor ratio over 1:1, the diffraction peak located at 2θ = 12.5° is originated from PbI_2, indicating the existence of unreacted PbI_2 crystal impurities in $CH_3NH_3PbI_3$ film. As the precursor ratio changes from 1:0.8 to 1:1.2, XRD pattern suggest that peak intensity of perovskite film at 2θ = 14.1° (indexed to (110) and (220) planes) decreases and strong (112)/(220) and (224)/(440) plane of $CH_3NH_3PbI_3$ crystals (at 2θ = 19.8° and 40.5°, respectively) dominates,[22] implying that the orientation of perovskite crystals is relevant to the film morphologies (needle-like vs flower-like) manipulated by varying the precursor composition. From the analysis above, the observed flower-like perovskite crystal with coverage of large grain domain is prerequisite for high efficient photovoltaic devices.[22] The *J-V* curves for device with different precursor ratios are shown in Figure 4, and Table 1 summarizes the extracted photovoltaic parameters. As a result, it is observed that the cell using equal molar amounts of PbI_2:CH_3NH_3I absorber has large crystal domains and (112)/(220) and (224)/(440) crystalline orientation are beneficial for transport of photogenerated carriers, leading to achieving increased photocurrent and highest *PCE*. Calculated substrate coverage percentages are 98.3% and 87.2% for 1:1 and 1:1.2 precursor ratio, respectively. Therefore,

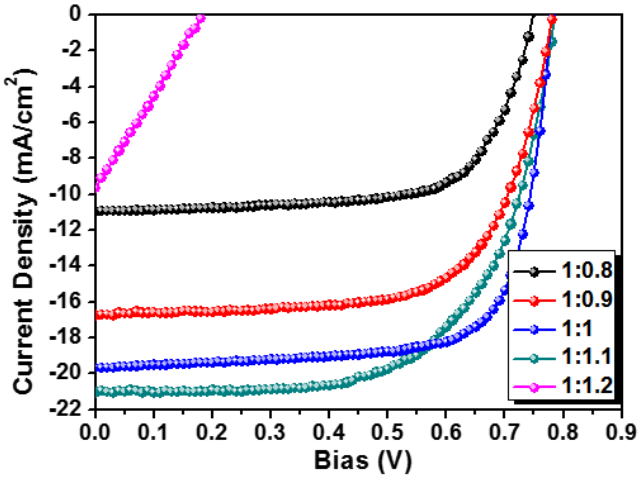

Figure 4. J-V curves of ultrasonic spray-coated $CH_3NH_3PbI_3$ solar cells made from 1:0.8, 1:0.9, 1:1, 1:1.1, and 1:1.2 PbI_2:CH_3NH_3I molar ratio solution.

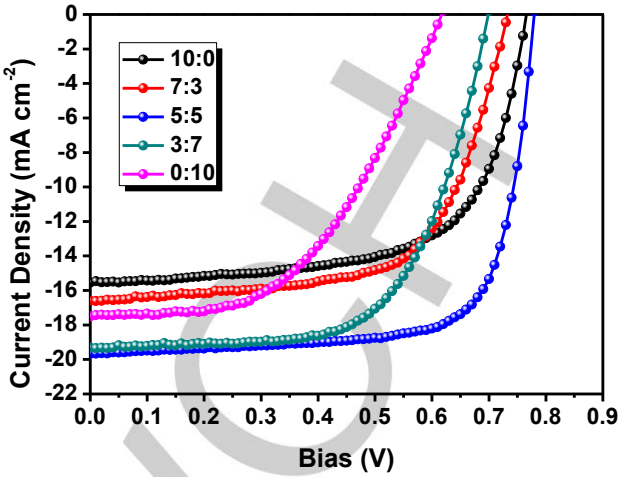

Figure 6. *J-V* curves of ultrasonic spray-coated $CH_3NH_3PbI_3$ solar cells made from DMSO:GBL solvent mixtures of 10:0, 7:3, 5:5, 3:7, and 0:10, respectively.

the low J_{sc} and V_{oc} value of $CH_3NH_3PbI_3$ film made from 1:1.2 precursor ratio are mainly due to the incomplete film coverage and large surface roughness. For PbI_2:CH_3NH_3I produced films with different ink formulations, the size and orientation of the perovskite domains may the key factors for explaining their different photoresponse.

After tuning the processing condition regarding the issue on precursor concentration and composition, the mixing solvents for the optimization of morphologies in ultrasonic spray-coated perovskite film were investigated in details through different volume ratios (10:0, 7:3, 5:5, 3:7 and 0:10) between DMSO and GBL as processing solvents for precursors comprised of 1:1 of PbI_2 and CH_3NH_3I. Figure 5 shows the top-view SEM images of perovskite films prepared from different mixing solvents. All the films exhibit similar dominated crystalline perovskite features from clusters of flower-like grains with length scale in the several ten to hundred micrometers, depending on the processing solvent composition. The crystal structures of perovskite made with

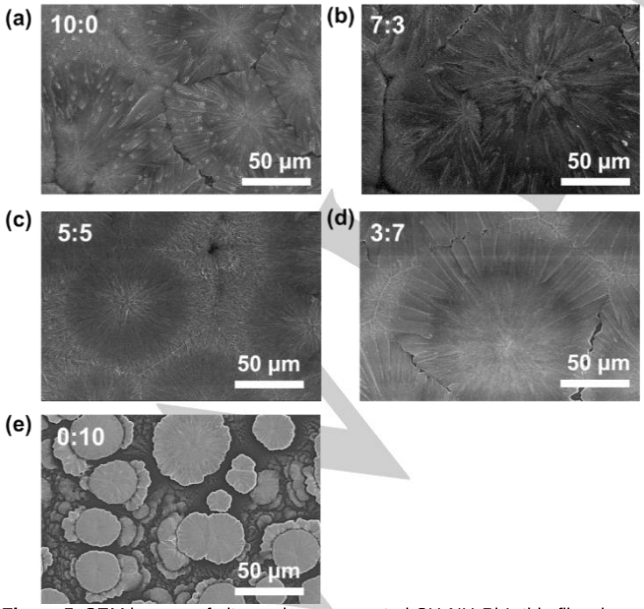

Figure 5. SEM images of ultrasonic spray-coated $CH_3NH_3PbI_3$ thin films based on DMSO:GBL solvent mixtures of (a) 10:0, (b) 7:3, (c) 5:5, (d) 3:7, and (e) 0:10.

different mixing solvents were formed in the same manner except for slight difference in diffraction intensities, as proved by the XRD patterns (Figure S5(a) of SI) with strong peak at a 19.8° and 40.5° assigned to (112)/(220) plane and (112)/(220). In the case of pure GBL, the cluster domain of perovskite is much smaller as compared to other solvent mixtures, and thus many voids are apparently observed on the crystal boundaries. In other words, the coverage of perovskite onto the top of the PEDOT:PSS underlying layer is relatively low (only ~74.7% coverage), which may deteriorate the device efficiency. A small quantity of DMSO addition into the GBL (ca. DMSO:GBL = 3:7) is helpful for formation of reasonably uniform and compact $CH_3NH_3PbI_3$ crystals predominately by sub-millimeter scale flower-like grains. The optimized microstructural morphology obtained from the DMSO:GBL solvent mixture of 5:5 creates interconnected large perovskite clusters which exhibit a higher optical absorbance in a broad visible and near-infrared region (Figure S5(b) of SI), whereas the poor perovskite film coverage made from pure GBL contributes to the reduction of absorption intensity especially in the low wavelength region (400~650 nm). *J-V* characteristics of the devices based on these different solvents of precursors were recorded in Figure 6. From the photovoltaic parameters summarized in Table 1, the optimized mixing solvents in a 5:5 ratio progressively lead to an enhancement in the J_{sc} and *FF*, and the resulting *PCE* is remarkably 2 and 1.5 times over the sample prepared from pure GBL and DMSO, respectively.

Finally, the formation and evolution process of ultrasonic spray-coated $CH_3NH_3PbI_3$ films during the post-thermal annealing process were investigated with regulated processing conditions discuss above (15% precursor concentration and 1:1 precursor molar ratio and 5:5 MAI:DMSO mixing solvent composition). It is found that the thermal annealing affects the perovskite thin film morphology and the corresponding device performance. Therefore, the as-fabricated films were annealed at temperatures varying from 90 °C to 130 °C for a fixed annealing duration of 30 min. SEM images in Figure 7 reveal distinctly different perovskite crystal morphologies depending on the annealing conditions. When the annealing temperature is much lower than the boiling points of mixing solvents (for example, under 90 °C), thin film surface displays the discontinuous needle-like domain. We observed a morphological transition from needle-like to flower-like

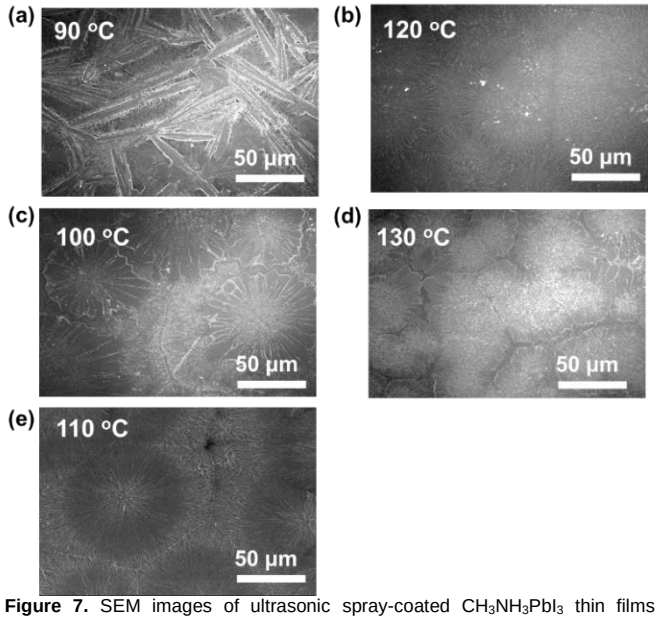

Figure 7. SEM images of ultrasonic spray-coated $CH_3NH_3PbI_3$ thin films annealed at (a) 90 °C, (b) 100 °C, (c) 110 °C, (d) 120 °C, and (e) 130 °C.

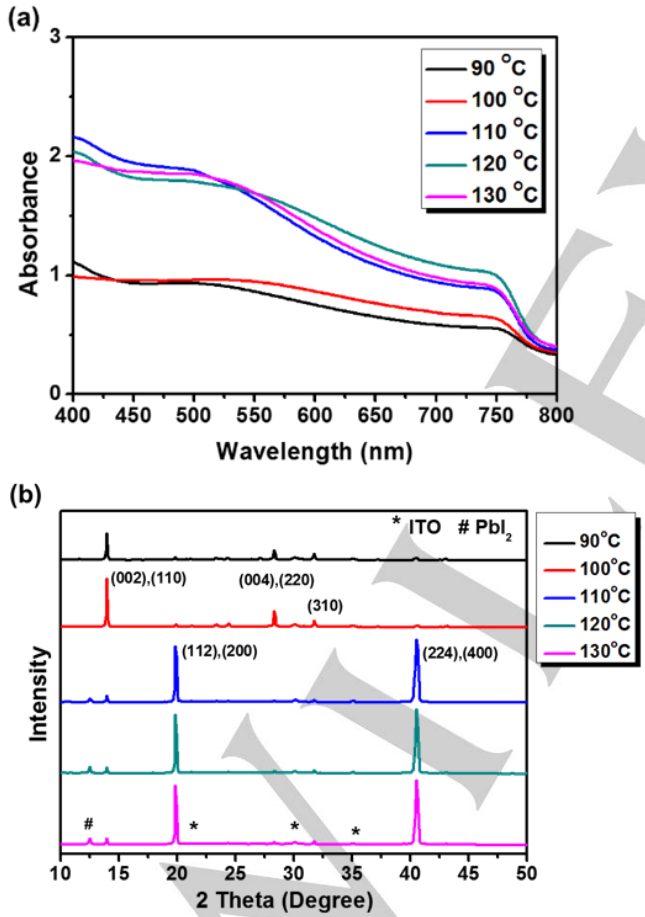

Figure 8. (a) Absorption spectrum and (b) XRD patterns of ultrasonic spray-coated $CH_3NH_3PbI_3$ thin films thermally annealed at 90 °C, 100 °C, 110 °C, 120 °C, and 130 °C, respectively.

when the annealing temperature is enhanced up to 100 °C. Very different morphology consisting of large flower-like crystal domains with less grain boundaries emerges as the annealing temperature further increases over 110 °C. The UV-Vis absorption at the range of 90 °C to 130 °C (see Figure 8(a)) show the typical absorption spectrum of perovskite $CH_3NH_3PbI_3$ films. Increasing the annealing temperature from 90 °C to 110 °C shows a significant increase in the absorbance across the whole spectral range. Further increasing the annealing temperature leads to similar absorbance without obvious change. To ensure that the morphological transformation among all the perovskite thin films can be correlated with the crystal structure properties, XRD spectra of $CH_3NH_3PbI_3$ films deposited by ultrasonic spray-coating and annealed by different temperatures were also examined (Figure 8(b)). All the films are converted into perovskite after thermal annealing but the peaks at 14.1° and 28.3° for the annealed film at 90 °C and 100 °C represent $CH_3NH_3PbI_3$ (110) and (220), respectively, whereas there are higher intensity of other planes, particularly (112)/(200) and (224)/(400), for the annealed perovskite film prepared at more than 110 °C, indicating that preferred grain orientation is different and highly related to the post-annealing temperature. Most importantly, the crystal plane difference can be interpreted in the disparate morphologies. When the crystals of CH_3NH_3I-PbI_2-DMSO complexes are heated at a lower temperature, the complexes are reasonably solidified and then a (100) peak of $CH_3NH_3PbI_3$ at 14.1° grows leading to the tree-like morphology.[22] The solvent at elevated temperature is evaporated without formation of intermediate complexes which influences the orientation of formed $CH_3NH_3PbI_3$ grain. As a result flower-like morphology is developed and strongly oriented along (112) and (200) direction.[22] In this condition (annealing at 110 °C), cross-sectional SEM image of a finished inverted planar perovskite solar cell with a device architecture of ITO/PEDOT:PSS/$CH_3NH_3PbI_3$/C_{60}/BCP/Ag shows a ~450 nm-thick compact $CH_3NH_3PbI_3$ layer with reduced grain boundaries (Figure S6 of SI). The *J-V* curves in Figure 9 exhibit the solar cell performance with response to V_{oc}, J_{sc}, *FF* and *PCE*, as summarized in Table 1. Compared between the different annealing protocols, the optimized perovskite film heated at 110 °C performs champion device with *PCE* of 11.30% with high *FF* of 73.6% likely due to the formation of highly-oriented large-sized flower-like perovskite crystallites.

All the above photovoltaic parameters were recorded in the forward scan when the voltage is swept form negative (short

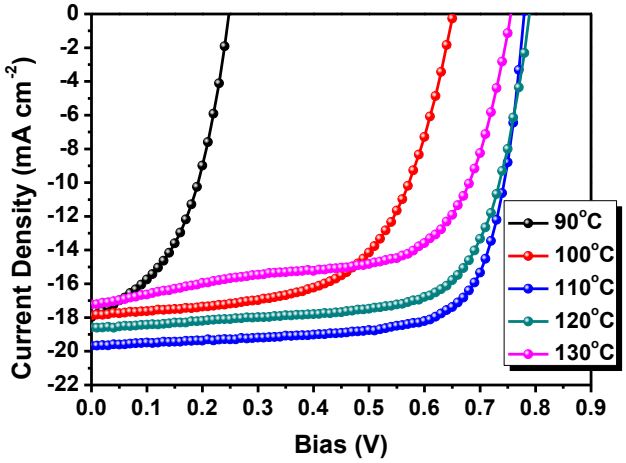

Figure 9. *J-V* curves of ultrasonic spray-coated $CH_3NH_3PbI_3$ solar cells thermally annealed at 90 °C, 100 °C, 110 °C, 120 °C, and 130 °C, respectively.

circuit) to positive (open circuit) at a scan rate of 0.1 V s^{-1}. The reverse scanning direction (backward scan) was also applied for analyzing the hysteresis phenomenon during the solar cell operation. Slight photocurrent hysteresis properties in this inverted ITO/ PEDOT:PSS/$CH_3NH_3PbI_3$/C_{60}/BCP/Al device were present in Figure S7 of SI probably due to the trapping state of the interface between the perovskite layer produced by ultrasonic spray-coating and top C_{60} passivation layer. Figure S8 of SI shows the EQE spectrum and its corresponding integrated J_{sc} over solar spectrum for this champion device cell. The EQE spectrum with a wide photoresponse (peaks values of 80% and broad band conversion efficiency exceeding 60% at wavelength of more than 750 nm) is in good agreement with absorption spectrum (Figure 8(a)) of the device fabricated in same condition. The integrated J_{sc} reaches 18.05 mA cm^{-2}, which is in accordance with measured J_{sc} (only within 10% lower) obtained from the *J-V* curve. Collectively, it is anticipated that the ultrasonic spray-coating technique performed in air with advantages such as facile and easy operating and cost-effectiveness makes it potential for the industrially scalable solution deposition methodology of the perovskite solar cells.

Conclusions

In summary, we have demonstrated the ultrasonic spray-coated $CH_3NH_3PbI_3$-based perovskite solar cells with one-step deposition method, which can be optimized through changing the total concentrations and stoichiometric ratios of precursor solution, mixing solvents and post-annealing temperatures. By understanding the processing conditions, it is found that the morphologies and crystalline orientation are both critical to manipulate the device efficiency. Employing an optimized condition based on 15% and 1:1 PbI_2:CH_3NH_3I precursor solution, 5:5 DMSO:GBL solvent mixture and treatment by 30 min of thermal annealing at 110 °C, the champion performing cell with the large grain (sub-millimeter scale in size) and full covering flower-like perovskite absorber (thickness~450 nm) has achieved a *PCE* of higher than 11%, which is one of the best performance records of spray-coated perovskite solar cells. Since such ultrasonic spray deposition technique can be easily adopted for large scale perovskite cells and integrated with roll-to-roll mass production, the study based on ultrasonic spray-coated large area perovskite film with good uniformity and reproducibility and its device application is now still ongoing.

Experimental Section

Materials. All the chemical reagents were purchased from commercial suppliers and used as received, unless stated otherwise. The methylammonium iodide (CH_3NH_3I) powder was prepared according to the previous report[49] and kept in N_2-filled glovebox before use.

Device Fabrication and Characterization. The planar perovskite solar cells were prepared with the basis structures of ITO/PEDOT:PSS/$CH_3NH_3PbI_3$/C_{60}/bathocuproine (BCP)/Ag. ITO glass substrates (1.5 cm × 1.5 cm) were ultrasonically cleaned with detergent, deionized water, acetone, and ethanol for 15 each and blow-dried in nitrogen, followed by oxygen plasma treatment for 5 min. A thin layer (~30 nm) of PEDOT:PSS (Clevious Al 4083) was deposited by spin-coating at 5000 rpm for 60 s and subsequently annealed at 120 °C for 20 min. The perovskite precursor solution was prepared by mixing PbI_2 and CH_3NH_3I at various molar ratios of 1:0.8, 1:0.9, 1:1, 1:1.1, and 1:1.2 in cosolvent system of dimethylsulfoxide (DMSO):γ-butyrolactone (GBL) (volume ratio of 10:0, 7:3, 5:5, 3:7, and 0:10) with a total concentration of 9~21 wt%. The photoactive perovskite layer were ultrasonic spray-coated onto PEDOT:PSS film in ambient atmosphere (relative humidity: 40~55 %) with heating the substrate at 70 °C through a commercial ultrasonic nozzle (Sono-Tek; with power of 0.2 kW and frequency of 80 kHz). The customized spray head driving system features programmable 3-axes coordinated motion via servomotors. The distance between nozzle and substrate in Z direction is at a constant 4 cm. The nozzle walks along the Y direction with a moving speed of 2 cm s^{-1}. The syringe pump controls the flow rate (~11.1 μl s^{-1}) of the mixing solution that is injected into the nozzle, whereas the pressure of air flow is fixed at 0.01 mPa. The as-deposited perovskite films were thermally post-annealed at 90~130 °C for 30 min in N_2-filled glovebox. Finally the solar cells devices were finished by thermal evaporation of C_{60} (20 nm), BCP (7 nm), and Ag (100 nm) at a chamber pressure of 10^{-6} torr. The effective area of each photovoltaic device cell was 4 mm^2 defined by aperture mask. Current density-voltage (*J-V*) curves under illumination were measured by applying an external voltage bias to the cell and recording the photocurrent with Keithley 2400 programmable source meter. A light source integrated with a Xe lamp with an illumination power of 100 mW cm^{-2} was used as solar simulator (provided by Enli Technology Co. Ltd.), calibrated by a Si reference cell. All the measurements were carried out in air without encapsulation. The EQE data were obtained by a spectral response/quantum efficiency measurement system (Enli Technology Co. Ltd.). Statistical analysis in photovoltaic parameters was deduced from at least 20 devices prepared in different batches.

Optical micrographs were obtained by Leica 2700M. UV-Vis spectrum was characterized by JASCO V-670 UV-Vis spectrophotometer. The scanning electron microscopy (SEM) was obtained from JEOL JSM-7600F The coverage percentage of ultrasonic spray-coated perovskite film is quantified using ImageJ software, to calculate the fraction of perovskite in SEM images. X-ray diffraction (XRD) analysis was performed on Bruker D8A X-ray diffractometer with a Cu Kα radiation.

Acknowledgements

The authors acknowledge the financial support from Ministry of Science and Technology of Taiwan (MOST).

Keywords: Perovskite • solar cell • ultrasonic spray-coating • one-step • solution-processing

[1] A. Kojima, K. Teshima, Y. Shirai, T. Miyasaka *J. Am. Chem. Soc.* **2009**, *131*, 6050-6051.
[2] H. S. Kim, C. R. Lee, J. H. Im, K. B. Lee, T. Moehl, A. Marchioro, S. J. Moon, R. Humphry-Baker, J. H. Yum, J. E. Moser, M. Gratzel, N. G. Park *Sci. Rep.* **2012**, *2*, 591.
[3] W. S. Yang, J. H. Noh, N. J. Jeon, Y. C. Kim, S. Ryu, J. Seo, S. I. Seok *Science*. **2015**, *348*, 1234-1237.
[4] X. Li, D. Q. Bi, C. Y. Yi, J. D. Decoppet, J. S. Luo, S. M. Zakeeruddin, A. Hagfeldt, M. Gratzel *Science*. **2016**, *353*, 58-62.
[5] M. Petrovic, V. Chellappan, S. Ramakrishna *Solar Energy*. **2015**, *122*, 678-699.
[6] M. Habibi, F. Zabihi, M. R. Ahmadian-Yazdi, M. Eslamian *Renewable Sustainable Energy Rev.* **2016**, *62*, 1012-1031.

[7] T. Salim, S. Y. Sun, Y. Abe, A. Krishna, A. C. Grimsdale, Y. M. Lam *J. Mater. Chem. A*. **2015**, *3*, 8943-8969.
[8] Z. G. Xiao, Y. B. Yuan, Q. Wang, Y. C. Shao, Y. Bai, Y. H. Deng, Q. F. Dong, M. Hu, C. Bi, J. S. Huang *Mater. Sci. Eng. R*. **2016**, *101*, 1-38.
[9] H. S. Jung, N. G. Park *Small*. **2015**, *11*, 10-25.
[10] Z. G. Xiao, C. Bi, Y. C. Shao, Q. F. Dong, Q. Wang, Y. B. Yuan, C. G. Wang, Y. L. Gao, J. S. Huang *Energy Environ. Sci.* **2014**, *7*, 2619-2623.
[11] S. Y. Sun, T. Salim, N. Mathews, M. Duchamp, C. Boothroyd, G. C. Xing, T. C. Sum, Y. M. Lam *Energy Environ. Sci.* **2014**, *7*, 399-407.
[12] W. Y. Nie, H. H. Tsai, R. Asadpour, J. C. Blancon, A. J. Neukirch, G. Gupta, J. J. Crochet, M. Chhowalla, S. Tretiak, M. A. Alam, H. L. Wang, A. D. Mohite *Science*. **2015**, *347*, 522-525.
[13] H. P. Zhou, Q. Chen, G. Li, S. Luo, T. B. Song, H. S. Duan, Z. R. Hong, J. B. You, Y. S. Liu, Y. Yang *Science*. **2014**, *345*, 542-546.
[14] J. Burschka, N. Pellet, S. J. Moon, R. Humphry-Baker, P. Gao, M. K. Nazeeruddin, M. Gratzel *Nature*. **2013**, *499*, 316-319.
[15] M. D. Xiao, F. Z. Huang, W. C. Huang, Y. Dkhissi, Y. Zhu, J. Etheridge, A. Gray-Weale, U. Bach, Y. B. Cheng, L. Spiccia *Angew. Chem. Int. Ed.* **2014**, *53*, 9898-9903.
[16] K. Wang, C. Liu, P. C. Du, L. Chen, J. H. Zhu, A. Karim, X. Gong *Org. Electron.* **2015**, *21*, 19-26.
[17] Q. Wang, Y. C. Shao, Q. F. Dong, Z. G. Xiao, Y. B. Yuan, J. S. Huang *Energy Environ. Sci.* **2014**, *7*, 2359-2365.
[18] H. Yu, F. Wang, F. Y. Xie, W. W. Li, J. Chen, N. Zhao *Adv. Funct. Mater.* **2014**, *24*, 7102-7108.
[19] N. J. Jeon, J. H. Noh, W. S. Yang, Y. C. Kim, S. Ryu, J. Seo, S. I. Seok *Nature*. **2015**, *517*, 476-480.
[20] Y. H. Deng, E. Peng, Y. C. Shao, Z. G. Xiao, Q. F. Dong, J. S. Huang *Energy Environ. Sci.* **2015**, *8*, 1544-1550.
[21] Y. G. Rong, Z. J. Tang, Y. F. Zhao, X. Zhong, S. Venkatesan, H. Graham, M. Patton, Y. Jing, A. M. Guloy, Y. Yao *Nanoscale*. **2015**, *7*, 10595-10599.
[22] S. Bae, S. J. Han, T. J. Shin, W. H. Jo *J. Mater. Chem. A*. **2015**, *3*, 23964-23972.
[23] H. B. Kim, H. Choi, J. Jeong, S. Kim, B. Walker, S. Song, J. Y. Kim *Nanoscale*. **2014**, *6*, 6679-6683.
[24] N. J. Jeon, J. H. Noh, Y. C. Kim, W. S. Yang, S. Ryu, S. Il Seol *Nat. 3Mater.* **2014**, *13*, 897-903.
[25] G. E. Eperon, V. M. Burlakov, P. Docampo, A. Goriely, H. J. Snaith *Adv. Funct. Mater.* **2014**, *24*, 151-157.
[26] A. Dualeh, N. Tetreault, T. Moehl, P. Gao, M. K. Nazeeruddin, M. Gratzel *Adv. Funct. Mater.* **2014**, *24*, 3250-3258.
[27] M. Saliba, K. W. Tan, H. Sai, D. T. Moore, T. Scott, W. Zhang, L. A. Estroff, U. Wiesner, H. J. Snaith *J. Phys. Chem. C*. **2014**, *118*, 17171-17177.
[28] Z. G. Xiao, Q. F. Dong, C. Bi, Y. C. Shao, Y. B. Yuan, J. S. Huang *Adv. Mater.* **2014**, *26*, 6503-6509.
[29] J. Liu, C. Gao, X. L. He, Q. Y. Ye, L. Q. Ouyang, D. M. Zhuang, C. Liao, J. Mei, W. M. Lau *ACS Appl. Mater. Interfaces*. **2015**, *7*, 24008-24015.
[30] H. Kim, K. G. Lim, T. W. Lee *Energy Environ. Sci.* **2016**, *9*, 12-30.
[31] J. J. Shi, X. Xu, D. M. Li, Q. B. Meng *Small*. **2015**, *11*, 2472-2486.
[32] C. C. Chueh, C. Z. Li, A. K. Y. Jen *Energy Environ. Sci.* **2015**, *8*, 1160-1189.
[33] A. T. Barrows, A. J. Pearson, C. K. Kwak, A. D. F. Dunbar, A. R. Buckley, D. G. Lidzey *Energy Environ. Sci.* **2014**, *7*, 2944-2950.
[34] K. M. Boopathi, M. Ramesh, P. Perumal, Y. C. Huang, C. S. Tsao, Y. F. Chen, C. H. Lee, C. W. Chu *J. Mater. Chem. A*. **2015**, *3*, 9257-9263.
[35] A. K. Chilvery, P. Guggilla, A. K. Batra, D. D. Gaikwad, J. R. Curried *J. Photon. Energy*. **2015**, *5*, 053093.
[36] S. Das, B. Yang, G. Gu, P. C. Joshi, I. N. Ivanov, C. M. Rouleau, T. Aytug, D. B. Geohegan, K. Xiao *ACS Photon.* **2015**, *2*, 680-686.
[37] S. Gamliel, A. Dymshits, S. Aharon, E. Terkieltaub, L. Etgar *J. Phys. Chem. C*. **2015**, *119*, 19722-19728.
[38] F. M. Li, C. X. Bao, H. Gao, W. D. Zhu, T. Yu, J. Yang, G. Fu, X. X. Zhou, Z. G. Zou *Mater. Lett.* **2015**, *157*, 38-41.
[39] Z. R. Liang, S. H. Zhang, X. Q. Xu, N. Wang, J. X. Wang, X. Wang, Z. N. Bi, G. Xu, N. Y. Yuan, J. N. Ding *RSC Adv.* **2015**, *5*, 60562-60569.
[40] M. Ramesh, K. M. Boopathi, T. Y. Huang, Y. C. Huang, C. S. Tsao, C. W. Chu *ACS Appl. Mater. Interfaces*. **2015**, *7*, 2359-2366.
[41] P. S. Chandrasekhar, N. Kumar, S. K. Swami, V. Dutta, V. K. Komarala *Nanoscale*. **2016**, *8*, 6792-6800.
[42] Y. S. Jung, K. Hwang, F. H. Scholes, S. E. Watkins, D. Y. Kim, D. Vak *Sci. Rep.* **2016**, *6*, 20357.
[43] F. M. Li, C. X. Bao, W. D. Zhu, B. H. Lv, W. G. Tu, T. Yu, J. Yang, X. X. Zhou, Y. R. Q. Wang, X. Y. Wang, Y. Zhou, Z. G. Zou *J. Mater. Chem. A*. **2016**, *4*, 11372-11380.
[44] F. Shao, L. Xu, Z. L. Tian, Y. Xie, Y. M. Wang, P. Sheng, D. L. Wang, F. Q. Huang *RSC Adv.* **2016**, *6*, 42377-42381.
[45] J. G. Tait, S. Manghooli, W. Qiu, L. Rakocevic, L. Kootstra, M. Jaysankar, C. A. M. de la Huerta, U. W. Paetzold, R. Gehlhaar, D. Cheyns, P. Heremans, J. Poortmans *J. Mater. Chem. A*. **2016**, *4*, 3792-3797.
[46] J. X. Wang, J. L. Li, X. Q. Xu, Z. N. Bi, G. Xu, H. L. Shen *RSC Adv.* **2016**, *6*, 42413-42420.
[47] X. Xia, W. Y. Wu, H. C. Li, B. Zheng, Y. B. Xue, J. Xu, D. W. Zhang, C. X. Gao, X. Z. Liu *RSC Adv.* **2016**, *6*, 14792-14798.
[48] D. K. Mohamad, J. Griffin, C. Bracher, A. T. Barrows, D. G. Lidzey *Adv. Energy Mater.* **2016**, *6*, 1600994.
[49] J. H. Im, C. R. Lee, J. W. Lee, S. W. Park, N. G. Park *Nanoscale*. **2011**, *3*, 4088-4093.

WILEY-VCH

Entry for the Table of Contents (Please choose one layout)

Layout 1:

FULL PAPER

This study investigates novel film deposition technique, ultrasonic spray-coating, for use in photoactive layer of perovskite solar cell via manipulating the ink formulation and the drying kinetic.

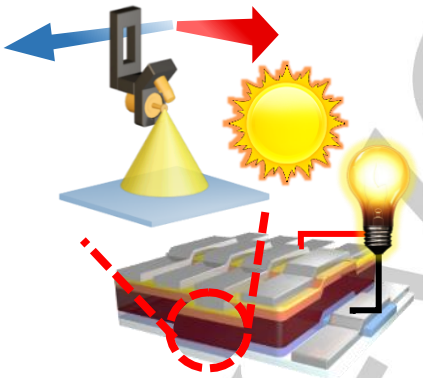

*Wei-Chieh Chang, Ding-Hung Lan, Kun-Mu Lee, Xiao-Feng Wang, Cheng-Liang Liu**

Page No. – Page No.

Perovskite Solar Cells Using Ultrasonic Spray-Coating Photoactive Layers